Electronic transport descriptors for the rapid screening of thermoelectric materials

SCHOLARONE™
Manuscripts

New Concepts

In this work, we show for the first time with the aid of first principles thermoelectric simulations of charge scattering in highly doped semiconductors polar optical phonon scattering plays a substantial role. Then, we utilize the scattering time calculations in the emerging class of ABX_2 compounds to discover transport descriptors for both charge mobility and thermoelectric power factor that we expect to be widely utilized for screening of potential new thermoelectric materials, especially with the availability of calculated databases. We believe that this significantly advances the state-of-the-art: while general principles in terms of band structure of promising thermoelectric materials are known (band degeneracy, lower effective masses etc), the role of hard-to-calculate carrier relaxation times is often ignored, largely because of a lack of accurate, yet rapid calculations of scattering times. Our work not only introduces a framework for such calculations, but can be broadly applied to functional inorganic materials design, beyond thermoelectrics in photovoltaics and high-power electronics.

Electronic transport descriptors for the rapid screening of thermoelectric materials

Tianqi Deng[1*], Jose Recatala-Gomez[2,3*], Masato Ohnishi[4*], D. V. Maheshwar Repaka[3*], Pawan Kumar[3], Ady Suwardi[3], Anas Abutaha[3,5], Iris Nandhakumar[2], Kanishka Biswas[6], Michael B. Sullivan[1], Gang Wu[1], Junichiro Shiomi[4#], Shuo-Wang Yang[1#], Kedar Hippalgaonkar[3,7#]

1 Institute of High Performance Computing, Agency for Science, Technology and Research (A*STAR), 1 Fusionopolis Way, Singapore 138632, Republic of Singapore

2 Department of Chemistry, University of Southampton, University Road, Highfield, Southampton SO17 1BJ, United Kingdom

3 Institute of Materials Research and Engineering, Agency for Science, Technology and Research (A*STAR), 2 Fusionopolis Way, Singapore 138634, Republic of Singapore

4 Department of Mechanical Engineering, The University of Tokyo, Hongo 7-3-1, Bunkyo-ku, Tokyo 113-8656, Japan

5 Qatar Environment and Energy Research Institute, Hamad Bin Khalifa University, Qatar Foundation, Doha, 34110, Qatar

6 New Chemistry Unit and School of Advanced Materials and International Centre for Materials Science, Jawaharlal Nehru Centre for Advanced Scientific Research (JNCASR), Bangalore 560064, India

7 School of Material Science and Engineering, Block N4.1, 50 Nanyang Avenue, Nanyang Technological University, Singapore 639798, Republic of Singapore

Abstract

The discovery of novel materials for thermoelectric energy conversion has potential to be accelerated by data-driven screening combined with high-throughput calculations. One way to increase the efficacy of successfully choosing a candidate material is through its evaluation using transport descriptors. Using a data-driven screening, we selected 12 potential candidates in the trigonal ABX_2 family, followed by charge transport property simulations from first principles. The results suggest that carrier scattering processes in these materials are dominated by ionised impurities and polar optical phonons, contrary to the oft-assumed acoustic-phonon-dominated scattering. Using these data, we further derive ground-state transport descriptors for the carrier mobility and the thermoelectric powerfactor. In addition to low carrier mass, high dielectric constant was found to be an important factor towards high carrier mobility. A quadratic correlation between dielectric constant and transport performance was established and further validated with literature. Looking ahead, dielectric constant can potentially be exploited as an independent criterion towards improved thermoelectric

37   performance. Combined with calculations of thermal conductivity including Peierls and inter-branch

38   coherent contributions, we conclude that the trigonal ABX_2 family has potential as high performance

39   thermoelectrics in the intermediate temperature range for low grade waste heat harvesting.

40

Introduction

42

43   The advent of machine learning (ML) and high-throughput (HT) density functional theory (DFT)

44   computation has shifted the scientific process from a time consuming Edisonian approach to a more

45   efficient, *in-silico* approach.[1–3] The deployment of these tools has led to multiple advancements:

46   prediction of novel compounds, either by HT-DFT[4] or ML,[5] that were later on realized experimentally

47   resulting in a knock-on effect of an acceleration of materials diagnosis,[6] and the fast screening of

48   promising material candidates[7–10] using materials descriptors, *i.e.* features that are inherent to the

49   material, easily calculated and have a direct relationship with a functional property.[11]

50   One widely used method for *ab initio* calculation of charge transport properties is the Boltzmann

51   transport equation (BTE).[12] The commonly adopted constant scattering time approximation (CSTA),

52   where a single, constant scattering time (τ_0) is assigned to all charge carriers,[13] is well-known for its

53   simplicity. However, such an inherent assumption is not always accurate in reality and depends on the

54   arbitrary choice of τ_0.[14,15] To bypass CSTA's shortcomings, researchers have employed the

55   deformation potential theory (DPT)[16] that adequately describes the electron-acoustic-phonon.[15,17–19]

56   More recently, an electron-phonon averaged (EPA) approximation has been introduced as an

57   alternative approximation, which includes both acoustic and optical phonon scattering and was

58   applied to half-Heusler alloys.[14] Nonetheless, the long-range Fröhlich-type scattering by polar optical

59   phonon (POP), which is particularly important for polar compound semiconductors,[20] is not included

60   in DPT or EPA approximations. Graziosi *et al.* have shown that inclusion of different electron-phonon

61   and ionized impurity scattering mechanisms could significantly alter the predicted thermoelectric

62   performance.[21,22] A recently developed approach, Energy-dependent Phonon- and Impurity-limited

63   Carrier Scattering Time AppRoximation (EPIC STAR), achieves good accuracy for polar materials at

64   lower computational cost and is therefore suitable for HT screening of such materials.[23] The Wannier

65 interpolation technique[24,25]enablesaccurate electron-phonon calculations as the state-of-the-art method

66 for phonon-limited charge transport properties predictions.[4,26–29] Yet it remains computationally

67 expensive due to large number of Brillouin zone sampling points needed for numerical

68 integration,[26,27]which is even more difficult for polar materials.[30–32] Therefore, an easy-to-compute

69 descriptor could facilitate rapid initial screening without performing complex computation for

70 materials with lower predicted potential.

71 One of the earliest HT-DFT study using first principles transport calculations was reported in 2008 by

72 Yang *et. Al,*[13]wherethey proposed LaPdBi as a new *n*-type thermoelectric material after screening

73 potential half-Heusler candidates with thermoelectric properties computed in CSTA. Similar methods

74 were also conducted by Raghuvanshi *et al.* to study the same class of materials.[33]Later on, based on

75 the work reported by Gautier *et. al.*[34], Zhou *et. al.*[4]conducted accurate electron-phonon calculations on

76 15 half-Heusler compounds, which led them to explain the large powerfactor in NbFeSb and ZrNiSn.

77 They also concluded that optical phonons are the dominant scattering mechanism for charges in many

78 half-Heuslers, in good agreement with available experimental data.[4]Zhu *et. al.*[35]performed stability

79 studies on half-Heuslers and predicted six stable compounds including TaFeSb, which is

80 experimentally synthesized and optimized to achieve a peak *zT* of ~1.52 at 973 K.[35]Other material

81 families have also been searched, such asgapped metals, clathrates, Chevrel phases and transition

82 metal dichalcogenides.[36–38]Xi and co-workers[15]screened the Materials Informatics Platform (MIP)

83 database and computed the electrical transport propertiesof161potential chalcogenides using DPT.

84 One of the candidates, $CdIn_2Te_4$ and its variations experimentally realized *zT*~1 at approximately 900

85 K.[15]Li *et al.* also screened the MIP for diamond-like ABX_2 compounds, and out of 41 candidates with

86 bandgap of 0.1-2.5 eV they predicted that 12 have high figure of merit (*zT*). And some of them were

87 experimentally realized, demonstrating the potential of these approaches.[39] These studied

88 demonstrated that incorporating relevant scattering mechanism in charge transport calculations is

89 necessary for reliably predicting the electrical transport properties. However, such high-throughput

90 scattering calculations are computationally demanding, and there is a long-standing lack of easy-to-

91 compute, general transport property descriptors as an alternative for materials screening.

92   Herein, we leverage upon the richness of the Materials Project (MP) Database[40], screening for

93   high symmetry, low band gap[41] chalcogenide compounds. From the MP Database, we focus on the

94   trigonal (space group number 166, $R\bar{3}m$) ABX_2 family where A and B are elements of alkali,

95   transition metals and group III and V, and X are chalcogens(S, Se, Te). ABX_2 compounds were

96   chosen due to their tendency to have low thermal conductivity, with the possibility of ns^2 lone pair

97   electrons,[42] which enabled us to narrow down our focus on charge transport properties. Our findings

98   reveal that in this family, polar optical phonon scattering, which has been neglected often in literature,

99   is significant even with heavy doping. We proposed charge transport descriptors based on ground

100   state properties and easy-to-obtain parameters. The descriptors described herein qualify themselves as

101   robust first level thermoelectric screening parameters, which obviate the need for computationally

102   expensive calculations. We expect this strategy to be widely implemented in the quest for high-

103   performance inorganic TE materials.

Materials informatics and candidate screening

105   We establish a screening strategy for the identification of unexplored potential TE candidates. To do

106   so, we first make use of appropriate material descriptors for the rapid assessment of key properties

107   directly correlated to the performance.[43] First, we screen for compounds with bandgaps lower than 4

108   eV, as it relates to the maximum Seebeck coefficient that can be achieved at a particular temperature (

109    $S_{max} \sim \frac{E_g}{2eT_{max}}$).[44] The thermodynamic stability as indicated by the energy above convex Hull is

110   evaluated at 0 K. At finite temperature (T > 0K), however, the contribution from configurational

111   entropy has been reported to stabilize compounds with $E_{Hull} > 0$. In other words, a small, non-zero

112   E_{Hull} at 0 K does not necessarily render experimental synthesis impossible ($E_{Hull} < 80meV$).[45,46] This is

113   confirmed by looking at the most recent entry for trigonal $AgBiS_2$ in the MP database (mp-29678),

114   which now shows $E_{Hull} \sim 20$ meV and has been experimentally realized.[47] Next, the number of charge

115   carrying valleys, or the valley degeneracy (N_v) is key to achieve high Seebeck coefficient and

116   electrical conductivity simultaneously, and is preferentially found in high symmetry structures.[48] We

117   set a threshold for compounds with more than four symmetry operations, thus increasing the

118   probability of having compounds with high N_v present in the dataset. Finally, to ensure data

119   sufficiency, we screened for binary, ternary and quaternary chalcogenides. Domain knowledge

120   motivates the choice of chalcogenide materials: traditionally, chalcogenides are good TE materials.[49–

121   55]Our screening resulted in nearly 600 compounds (combining binary, ternary and quaternary), from

122   which we focused on ternary chalcogenides, as they represent the majority fraction in the mined data.

123   Among all potentially stable, high symmetry chalcogenide compounds, we focus on a subset of the

124   screened compounds, while keeping the space group fixed.   In the end, the initial dataset was

125   comprised by 146 ternary chalcogenides with chemical formula $ABX_2$and trigonal structure(space

126   group $R\bar{3}m$). This initial dataset was reduced to 12 compounds after filtering out the low performing

127   candidates based on previously calculated CSTA powerfactors from Ricci *et al.*,[56]to compare CSTA

128   with our detailed scattering time calculations. In addition, it is noteworthy to mention that TE

129   properties have only been experimentally reported for3out of 12 compounds from our dataset (trigonal

130    $TlBiTe_2$, trigonal $TlSbTe_2$ and a different symmetry, cubic $AgBiS_2$), leaving an unexplored chemical

131   space.[57–61]While $AgBiS_2$with space group $R\bar{3}m$ has not been demonstrated, this intermediate phase

132   has been experimentally realized in $AgBiSe_2$.[62,63] Hence, it could be possible to achieve trigonal

133    $AgBiS_2$ in a similar fashion. *Ab initio* transport property simulations were then performed for these

134   12 compounds, and a pictorial representation of the computational framework deployed in this work

135   can be found in Figure 1. It is to be noted that while we use these 12 compounds to analyse and

136   produce transport descriptors, the methodology is expected to be generally applied to a larger class of

137   inorganic semiconductors; we restricted it only for the purposes of this work.
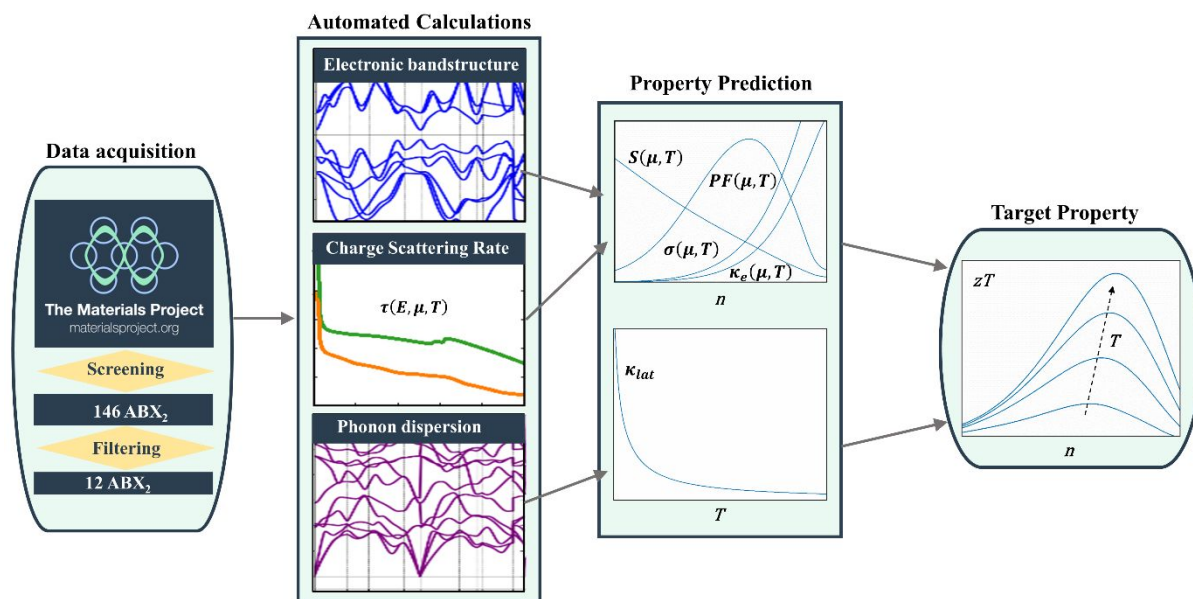
Figure 1. Computational framework deployed in this work. The electron band structure and DFPT phonon calculations of the 12 candidate compounds were carried out using QUANTUM ESPRESSO. Afterwards, charge transport properties were simulated using the EPIC STAR method, taking into consideration scattering events produced by both acoustic and optical phonons, ionized impurities and Thomas Fermi screening of free carriers.[23] Lattice thermal conductivities were calculated using phonon BTE and a unified theory implemented in ALAMODE, including 3-phonon scattering events and interbranch tunneling coherent contribution.[64]

138

Results and Discussion

139   Figure 2(a) shows the crystal structure for ABX_2 compounds, with space group $R\overline{3}m$ (No. 166). The

140

141   layered structure is comprised by [B-X] slabs in the *b-c* plane with A cations orthogonal to this plane

142   (along the *c*-axis). The atoms A and B occupy octahedral positions and interact with X with

143   dissimilar strength, depending on the ion charge and specific position they occupy in the slab. On the

144   other hand, the X atoms are octahedrally coordinated with respect to AB. To illustrate the bonding

145   nature and crystal symmetry, Figure 2(b) shows the DFT band structure for$AgBiS_2$, which has an

146   indirect bandgap of ~ 0.65 eV, where the valence band maxima is between the Γ and X high

147   symmetry points and the conduction band minima is centred at the Z point. According to the partial

148   density of states (PDOS), the valence band maxima is mainly comprised of sulphur p-states with

149   modest contribution from silver d-states, whilst the conduction band minima is mainly bismuth p-

150   states, with minor contributions from silver and sulphur. The phonon dispersion shown in Figure 2(c)

151   is comprised of three acoustic branches and nine optical branches, with the lowest optical phonon

152   located at $ca.50 cm^{-1}$. The proximity of the optical branches to the acoustic branches is expected to

153   lead to a decreased lattice thermal conductivity near room temperature, due to increased scattering

154   phase space and higher likelihood of phonon-phonon scattering. The phonon density of states in

155   Figure 2(c) shows the optical branches at low energy mainly comprised of vibrations of Ag atoms,

156   followed by vibrations of Bi atoms. Additional verification is given by the atomic participation ratio

157   (APR), which quantifies the degree of participation of different atoms in a specific phonon mode.[65]

158   We observe that Ag and Bi have a large participation ratio (red colour) in the phonon modes of the

159   lowest optical branches. In addition, these low-lying optical branches are flat and avoid crossing the

160   acoustic branches at certain high symmetry points of the Brillouin zone (for instance at the Γ and L

161   points). The combination of high participation ratio, flat low energy optical branches and avoided

162   crossing with acoustic branches hints at localized phonon vibration which would potentially decrease

163   the lattice thermal conductivity.[66]Further, ABX_2 compounds have attracted interest due to the

164   presence of lone-pair electrons, which are expected to result in softened phonon modes. Note that

165   experimentally synthesized $AgBiS_2$ results in the rock-salt disordered cubic Fm3-m space group,

166   different from our study of the R3-m space group. In rock-salt compounds with the ABX_2 formula,

167   the presence of ns^2-orbitals[67] induces structural instabilities that translate into an increase of

168   anharmonicity in the bonding, ultimately resulting in strong phonon-phonon interactions that can

169   potentially reduce the lattice thermal conductivity as low as the amorphous limit.[42]Figure 2(d) shows a

170   bar plot representing the theoretical thermoelectric performance for a range of temperatures, from

171   300K to 900K, for six out of the twelve n- and p-type ABX_2 chalcogenides, (note that thermal

172   conductivity calculations are more computationally expensive, hence were not performed on all 12

173   compounds). The thermoelectric figure-of-merit zT_{max} was calculated using lattice thermal

174   conductivity in the amorphous limit, while zT_{cryst} was calculated using lattice thermal conductivity

175   corresponding to perfectly crystalline samples (Figure S1(a)). In addition, we also calculated zT using

176   the lattice thermal conductivity for polycrystalline samples with grain size of 1 μm (Figure S1(a)) and

177 the resulting zT border the values of the single crystal samples (zT_{cryst}). This is because the phonon

178 mean free path is much smaller than 1 μm (see Figure S1(b)), so the impact of grain boundaries

179 becomes less relevant. In many cases, p-type ABX_2 compounds show higher thermoelectric

180 performance than their n-type counterpart, due to a high band degeneracy which is attributed to their
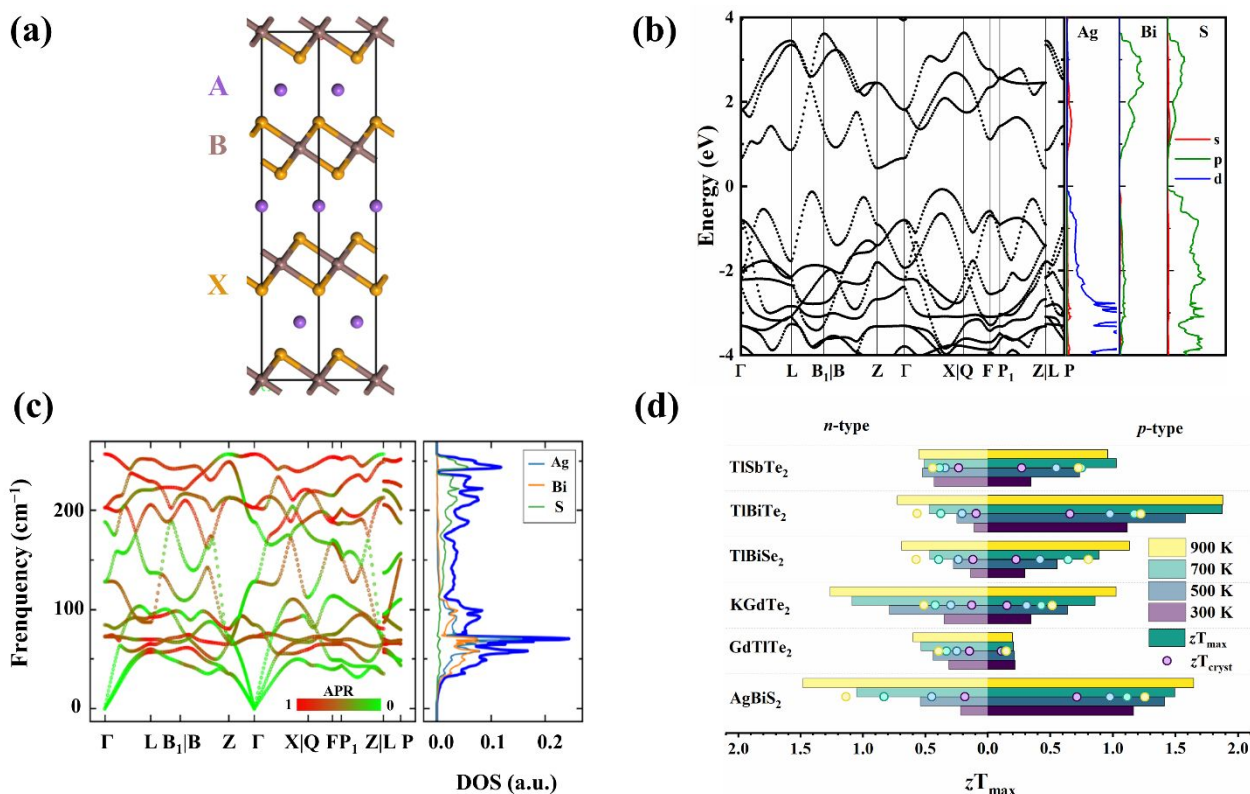
181 complex valence band structure.[9]

Figure 2. (a) Atomic structure of ABX_2 chalcogenides, (b) Calculated electronic band structure for $AgBiS_2$, (c) Calculated phonon dispersion for $AgBiS_2$.The colour of the bands denotes atomic participation ratio (APR), ranging from green (zero, no participation in the phonon mode) to red (one, large participation in the phonon mode).(d) Maximum zT (zT_{max}, bar graph) and zT for the single crystal sample (zT_{cryst}, circles) as a function of temperature for selected n- and p-type ABX_2chalcogenides. zT_{max} has been calculated employing the minimum lattice thermal conductivity (amorphous limit) while zT_{cryst} has been calculated for a single crystal by including three-phonon scattering.

182

183 Among these, the p-type $AgBiS_2$and $TlBiTe_2$ compounds could reach a zT above 1 at room

184 temperature. Especially, the predicted value for n-type $AgBiS_2$ is higher than the experimental results

185 obtained by Rathore et $al.$[47]This mismatch is likely because the optimal carrier concentration (1.48 ×

186   10^{19} cm^{-3} for *n*-type AgBiS$_2$ at room temperature) was not experimentally realized, and their synthesis

187   resulted in the cation-disordered cubic rock salt structure.[47]Their analysis also concluded that further

188   optimization of the carrier concentration through doping in *n*-type AgBiS$_2$was required to achieve

189   better performance. Interestingly, our calculations show the *p*-type TlBiTe$_2$ compound is expected to

190   achieve a maximum *zT* of ~1.9 at 900K, which is much larger than previously reported experimental

191   values for the material (0.15 at 760K), signifying the potential for further optimization.[57]Within the

192   ABX$_2$ family, the best performance is attained experimentally by the cubic *p*-type alloy

193   AgSbTe$_{1.85}$Se$_{0.15}$, with *zT* ~ 2 in the temperature range 550-600 K, mainly due to further reduction in

194   the thermal conductivity from point defects and stacking faults.[68] Recently, Roy Chowdhury *et al.*

195   have developed a strategy based on atomic disorder engineering in Cd-doped AgSbTe$_2$, reporting an

196   ultrahigh *zT* of ~*1.5* near–room temperature.[69]In fact, this material is also cubic (space group F$\overline{3}$dm)

197   as opposed to the trigonal (space group R$\overline{3}$m) ABX$_2$ compounds studied here, and it is not currently

198   contained in the Materials Project database, which explains its absence from the potential candidate

199   dataset resultant from the screening.[68]

200   We also study in detail the representative charge scattering mechanism that makes these compounds

201   good prospects for mid-temperature thermoelectric applications. Figure 3 shows the energy

202   dependence of the scattering rate for both *n*- and *p*-type AgBiS$_2$and TlBiTe$_2$at 300 K for the optimal

203   doping condition (determined from the peak of the powerfactor, S^{2}σ as a function of carrier

204   concentration). In general, the same scattering phenomena are dominant, from the energy

205   dependencies, for both *n*-type and *p*-type materials at 300 K. For these optimally doped materials,

206   ionised impurities dominate the charge scattering around the Fermi level (blue dash-dotted lines in

207   Figure 3). Interestingly, even in such a heavily doped regime where charge carrier scattering arising

208   from polar optical phonons is partially screened by the free carriers, we still observed a strong

209   contribution from optical phonons, that surpasses the acoustic phonon contribution. The contribution

210   from optical phonons is especially significant for *n*-type TlBiTe$_2$ [Figure 3(c)], comparable to that

211   from ionised impurities. Moreover, for high-energy carriers the optical phonon scattering even

212   dominates over ionized impurities. Similar trends are observed for the *p*-type materials, as shown in

213   Figure 3(b) and 3(d). This emphasizes the importance of polar optical phonon scattering, even in the

214   heavily doped case where free-carrier screening is strong.In fact, in both *n*-type and *p*-typeAgBiS$_2$and

215   TlBiTe$_2$, the overall scattering rate has a higher contribution from the optical phonons as compared to

216   the acoustic phonons, which is in stark contrast to the widely used assumption of acoustic-phonon-

217   dominated scattering in the literatures.[70,71]This signifies the importance of including the polar optical

218   phonon (POP) scattering contribution for polar materials, as this could potentially indicate the

219   dominance of POP despite high temperature and doping. Consequently, using acoustic phonon limited

220   assumption in analyzing the charge transport properties can result in substantial error, particularly in

221   ABX$_2$ as well as half Heusler class of compounds.[4]
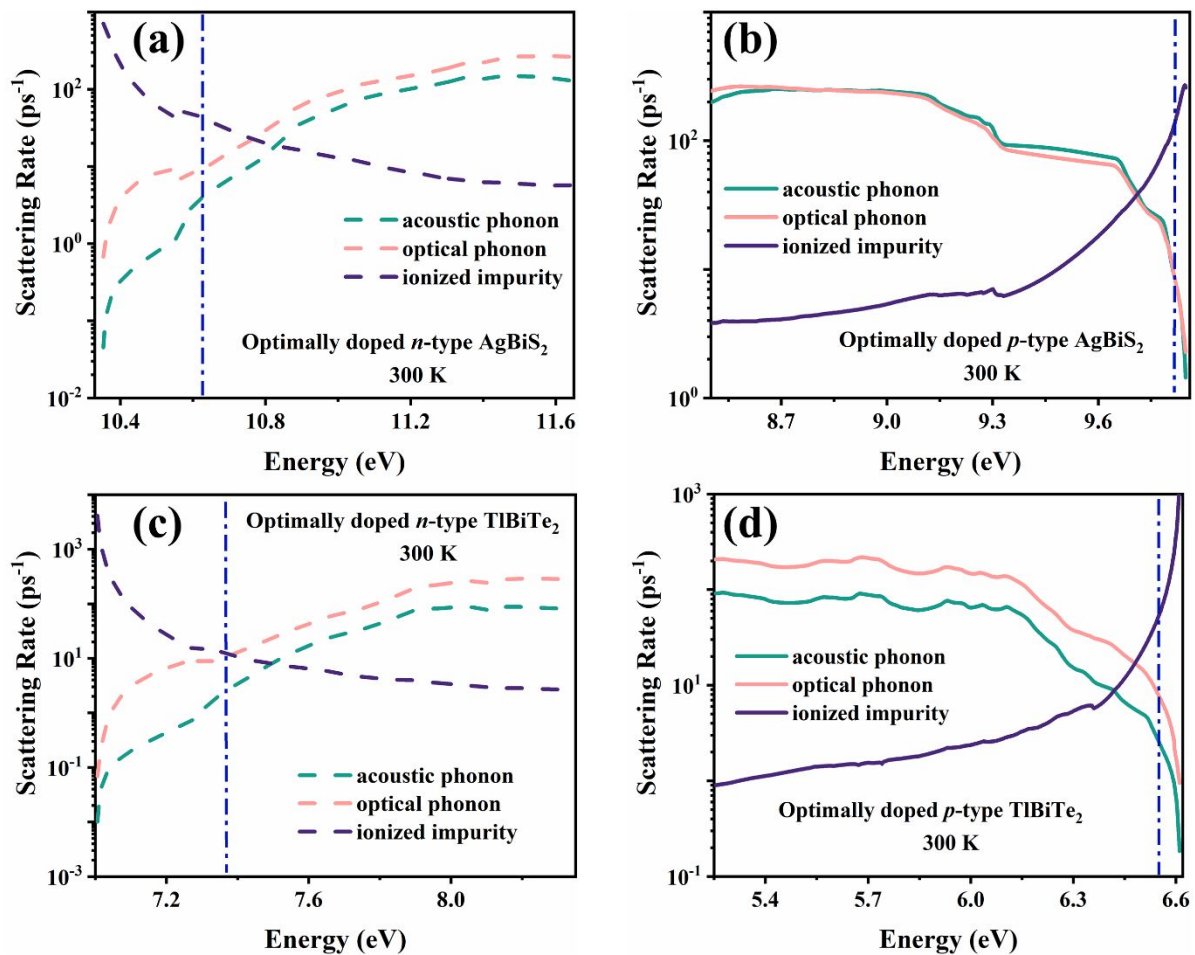

Figure 3. Room temperature scattering rate for optimally doped (a) *n*-type and (b) *p*-type AgBiS$_2$and (c) *n*-type and (d) *p*-type TlBiTe$_2$. The vertical blue line indicates the Fermi level at optimal doping level.

222

223   In light of this understanding, and to facilitate the rapid screening and identification of potential high-

224   performance thermoelectric materials, key descriptors which account for these scattering mechanisms

225   can be deduced. Previously the quality factor B proposed by Wang *et al.* has been adopted in the

226   screening for high performance thermoelectrics.[72] Nevertheless, this requires one key assumption: the

227   scattering is dominated by acoustic phonons throughout the doping and temperature range under

228   study. However, in our case of ABX_2 compounds, and possibly in other potential thermoelectric

229   materials, the B-factor would not qualify as a reasonable descriptor, as from Figure 3 we observed that

230   the charge scattering events are controlled by polar optical phonons and ionized impurities.

231   To derive such descriptors, we first observe that the POP scattering rate is proportional to the Fröhlich

232   coupling strength $\tau_{POP}^{-1}(E) \propto |C_{POP}|^2$, which in turn can be written as a function of Born effective

233   charge, phonon displacement and dielectric constant. Importantly, it is inversely proportional to the

234   dielectric constant via $C_{POP} \propto \frac{1}{\hat{q} \cdot \varepsilon \cdot \hat{q}}$.[20,73] Therefore, the POP scattering time should also be

235   proportional to dielectric constant squared $\tau_{POP}(E) \propto \varepsilon^2$. Similarly, the ionized impurity scattering

236   strength also depends on the dielectric constant as the charges also experience electrostatic

237   screening.[23,74] Therefore in the Brooks-Herring model, the scattering rate from ionized impurity is also

238   inversely proportional to dielectric constant squared $\tau_{IIS}(E) \propto \varepsilon^2$. Since the dielectric constant

239   determines the overall electrostatic interaction, we conjecture that the interaction strength for other

240   phonons may also be inversely correlated to ε. Furthermore, this assumption is advantageous, since a

241   small reduction in accuracy is traded for a simpler, easy-to-calculate descriptor. Hence, we focus on

242   the role of dielectric constant and hypothesize that the overall scattering rate should be strongly

243   correlated to ε^2 (further details in Supplementary Section 1). Thus, we propose a general transport

244   descriptor by considering mixed scattering contribution from ionized impurities and polar optical

245   phonons. The descriptor for the carrier mobility is obtained by applying the relation $\mu = \frac{e\tau}{m_C^*}$

246   considering that the total scattering time is proportional to ε^2:

247 $\mu \propto \varepsilon^2 m_C^{-1}$ (1)

11

248   where μ is the direction averaged mobility at optimal carrier concentration, m_c is the conductivity

249   effective mass, ε is the dielectric constant and T is the absolute temperature in K.

250   Figure 4(a) shows the correlation between the transport descriptor and the direction averaged mobility

251   for our calculated ABX_2 compounds. We benchmarked our data together with experimental values

252   from the literature, in order to validate the descriptor.[49–53,55,75] The temperature dependent effective

253   masses, conductivity effective masses and the dielectric constant were used when reported[50,52,53],

254   whereas for other compounds we used values reported in the Landolt–Börnstein database, e.g. for

255   effective mass for PbTe[76], or other literature e.g. for the dielectric constant of PbTe.[77] Interestingly,

256   materials of different crystal systems (*e.g.* cubic PbTe and orthorhombic SnSe) follow the same trend,

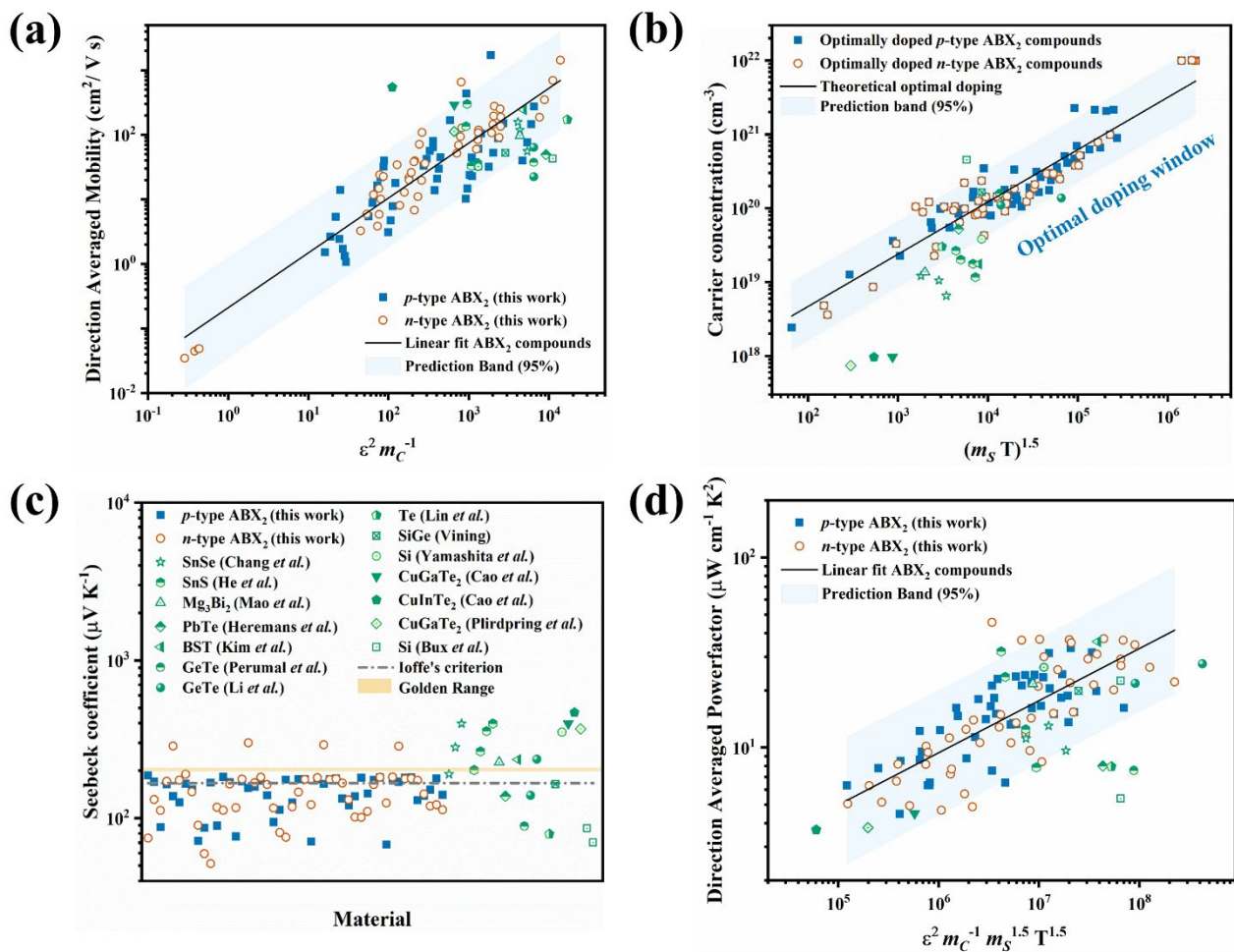257   hinting that the descriptor could be generally applicable.

Figure 4. Transport descriptors for ABX_2 materials. (a) Direction averaged mobility transport descriptor at

optimal doping. (b) Optimal carrier concentration (n_{opt}) descriptor.[78] (c) Seebeck coefficient for each

material (x-axis, ABX_2 materials are listed in alphabetical order) versus theoretical criteria (Ioffe's

criterion[79] and golden range[80]). (d) Direction averaged powerfactor transport descriptor at optimal doping.

The benchmark corresponds to experimental data.[49–53,55,75,81–83,84,85,86] The data was taken from the respective

references and averaged using the method described by Parker *et al.*[87] The blue area in (a), (b) and (d)

corresponds to the prediction band calculated for ABX_2 compounds. It corresponds to the range of values

that are likely to contain the value of a new observation, with a 95% confidence.

258

259   In additional to the carrier mobility, another key quantity in optimizing the thermoelectric

260   performance is the carrier concentration. Assuming a single carrier type, the optimal carrier

261   concentration (n_{opt}) should be proportional to the Seebeck effective mass and the temperature, $n_{opt} \propto$

262     $(m_S T)^{1.5}$.[78] In Figure 4(b), this trend is plotted for *n*- and *p*-type ABX_2 compounds as well as for the

263   literature values used for benchmark, at their corresponding carrier concentration. We observe that, as

264   expected, our compounds follow the trend whilst some literature values deviate from this ideal

265   relationship, indicating that the reported carrier concentration may not be at the optimal level.

266   Next, a descriptor for the powerfactor (PF = $S^2\sigma$; PF $\propto S^2 n\mu$) is derived, where the mobility

267   descriptor is given by Equation 1 and a descriptor for optimal carrier concentration is given by $n_{opt} \propto$

268     $(m_S T)^{1.5}$.[78]However, a descriptor for the Seebeck coefficient is not as readily available. The

269   underlying difficulty of finding a descriptor for the Seebeck coefficient resides in the fact that

270   theoretically, the Seebeck coefficient at optimal doping should be a constant.[88]This originates from

271   the steady-state solution to the BTE, that states that the optimal Seebeck coefficient only depends on

272   reduced Fermi potential and scattering exponent and thus, is independent of effective masses, the

273   valley degeneracy and scattering strength.[74] Hence, under the parabolic band approximation, the

274   powerfactor will be maximized at a single value of Seebeck coefficient, S_{opt}. This was first proposed

275   by Ioffe, who reported that the optimized value for Seebeck coefficient is 172 μV K^{-1}.[79] Later,

276   Pichanusakorn and Bandaru showed that S_{opt} can be found in a range of 130-187 μV K^{-1}and that the

277   most frequent value was 167 μV K^{-1}.[89] Recently, Hong *et al.* expanded on this issue by reporting that

278   the optimized Seebeck coefficient is not a single value but a range that changes depending on whether

279   we are optimizing zT or the powerfactor. The authors reported that to achieve maximum powerfactor,

280   the Seebeck values range from 195 µV K^{-1} to 202 µV K^{-1}.[80] The Seebeck tendency to accumulate

281   around a range of values has also been noted by Zhang *et al.*[90]Figure 4(c) shows the Seebeck

282   coefficient of our ABX$_2$ compounds along with the Seebeck coefficient of the literatures. Deviations

283   from the optimal value may be indicative of non-optimal doping. However, we observe that while the

284   majority of theoretical and experimental values of S approach the theoretically predicted limits, they

285   still span a wider range.

286   Nevertheless, we introduce a transport descriptor for the direction averaged powerfactor at optimal

287   doping (PF), shown in Equation 3. They key assumption is that the carrier concentration is given by

288   its optimal value (n = n$_{opt}$ $\propto$ (m$_S$ T)$^{1.5}$), while the Seebeck coefficient is around an optimal constant (S

289   ~ S$_{opt}$ ~ constant):

290
$$PF \propto \varepsilon^2 m_C^{-1} m_S^{1.5} T^{1.5} \qquad (3)$$

291   The comparison between PF and the descriptor are shown in Figure 4(d). We indeed observe an

292   increasing trend of PF with respect to the transport descriptor for both simulated *n*- and *p*-type ABX$_2$

293   compounds as well as for the literature, with some literature values deviating from the general trend.

294   This is a consequence of assuming optimal doping during the derivation of the PF descriptor: the

295   powerfactor of materials with non-optimal doping will be lower than the maximal power factor that

296   can be achieved. This also provides a theoretical guidance for experimental optimization of

297   thermoelectric performance via tuning the carrier concentration towards optimal doping level. The

298   good correlation between the transport descriptors and the transport properties potentially enable a

299   facile method for first-level screening of potential TE candidates from easy to calculate parameters.

300   In order to compare to the CSTA derived descriptors in Ricci *et al.*, we also observed that another

301   descriptor for the powerfactor, the Fermi surface complexity factor ($N_V^*K^*$, Figure S2)[9] indeed also

302   captures the trend. Importantly, our descriptor is related to $N_V^*K^*$, as it captures the band features, but

303   contains more information regarding the scattering rate, which is absent in $N_V^*K^*$due to the CSTA

304   assumption.

305   In addition, we also analyze phonon properties of these ABX_2 compounds to gain insights into

306   their phonon anharmonicity and instability, which lead to low thermal conductivities (Figure S3(a)).

307   In order to explore anharmonicity, Nielsen *et. al.*[42] used an applied electric field and displacement of

308   atoms, that significantly deform the lone-pair charge density of the group V element, resulting in the

309   structural instability and strong phonon anharmonicity of ABX_2 compounds. For materials composed

310   of guest atoms and a framework such as skutterudites[91,92] and clathrates[93], effects of phonon

311   anharmonicity can be analyzed by comparing phonon properties of the pristine structure and structure

312   excluding the guest atoms. One, however, cannot employ this approach for ABX_2 compounds because

313   removing the group V elements breaks the structure. In this analysis, we have applied hydrostatic

314   strains to ABX_2 compounds to tune its phonon anharmonicity.

315   Because the three-phonon scattering is a complicated process, we have carefully analyzed

316   change of harmonic and anharmonic terms on phonon relaxation times when such a strain was applied

317   to the system. Here, we analyzed $AgBiS_2$, which exhibits promising electronic powerfactor. As shown

318   in Figures 2(c) and 5(a), ABX_2 compounds have flat bands at low frequency. The most intuitive effect

319   of the flat band may be enhancement of Scatting Phase Space (SPS). SPSs of absorption (+) and

320   emission (-) processes, $P_3^{\pm}(q) = \left(\frac{1}{N}\right)\sum_{q_1 q_2}\delta(\omega \pm \omega_1 - \omega_2)\delta(q \pm q_1 - q_2 - G)$, have been computed

321   with and without including the effect of the lowest optical branch, one of the flat bands around 60-80

322   cm^{-1} shown as a bold line in Figure 5(a). This flat band increases SPS of absorption (emission)

323   process at frequencies lower (higher) than its frequency as shown in Figure 5(b). It is worth noting

324   that while the lone-pair electrons result in whole features of atomic vibrations rather than only in flat

325   bands, the flattening is one of the representative features of the lone-pairs resulting in weak bonding.

326   While the presence of flat bands may be related to the phonon anharmonicity and local

327   distortions, SPS is a harmonic phonon property. We have, therefore, applied a hydrostatic strain, a

328   uniform expansion, to the compound to explore its phonon anharmonicity. As shown in Figure 5(a),

329   transverse acoustic (TA) modes around T point, q = (0.5, 0.5, 0.5), are significantly modified by the

330   applied strain; their frequencies decrease and finally approaches imaginary values, which are

331   represented as negative values in Figure 5(a). The instability of TA modes on Γ-X line can be clearly

332   confirmed by the Grüneisen parameter, defined as the change in the frequency with the crystal volume,

333   as shown in Figure 5(c). Red markers in Figure 5(c) show values for TA modes on $q = (q, q, q)$, where

334   q is an arbitrary number, and the inset clearly shows that the value increases steeply as the T point is

335   approached. Furthermore, the instability becomes stronger at the accelerating rate under the strain as

336   shown in the right panel of Figure 5(c). It is also intriguing to see the eigenvector of the TA mode at T

337   point. In the TA mode at T point, bismuth atoms whose $6s^2$ orbitals form lone-pair electrons largely

338   move along the in-plane direction while silver atoms do not move and sulfur atoms move only slightly

339   (see Figure S3), which may result in strong distortion of charge distribution.

340   Because the changes in phonon dispersion and Grüneisen parameter clearly show that the TA

341   mode at T point is unstable and should have a strong anharmonicity, we analyze its three-phonon

342   interaction in detail. The detailed observation of the $|V_3|^2$ term described in the *Methods* section

343   clearly shows that this unstable phonon mode mainly interacts with phonon modes from the flat bands

344   around 60-80 cm^{-1} (see left panel in Figure S3(a)), and this interaction is enhanced by the applied

345   strain as shown in Figure 5(d). Although SPS of the TA mode is also changed because of the change

346   in its frequency with applied strain, its change is superseded by the change in the $|V_3|^2$ term as shown

347   in Figure S3. Enhancement of $|V_3|^2$ terms of low frequency modes due to flat bands has been also

348   observed in clathrate compounds.

349   These analyses reveal complicated but intriguing effects of the flat band; it enhances not only SPS but

350   also the three-phonon matrix elements, $|V_3|^2$, and furthermore is related to the phonon instability at

351   low frequency. Overall, the class of compounds has many intriguing possibilities with the low-lying

352   optical modes providing enhanced phonon anharmonic scattering, with polar optical phonon

353   scattering being dominant for majority carriers, therefore resulting in higher electronic powerfactor.

354   Thus, the expected zT for optimally doped ABX$_2$ compounds is >1 at intermediate to high

355   temperatures.

356
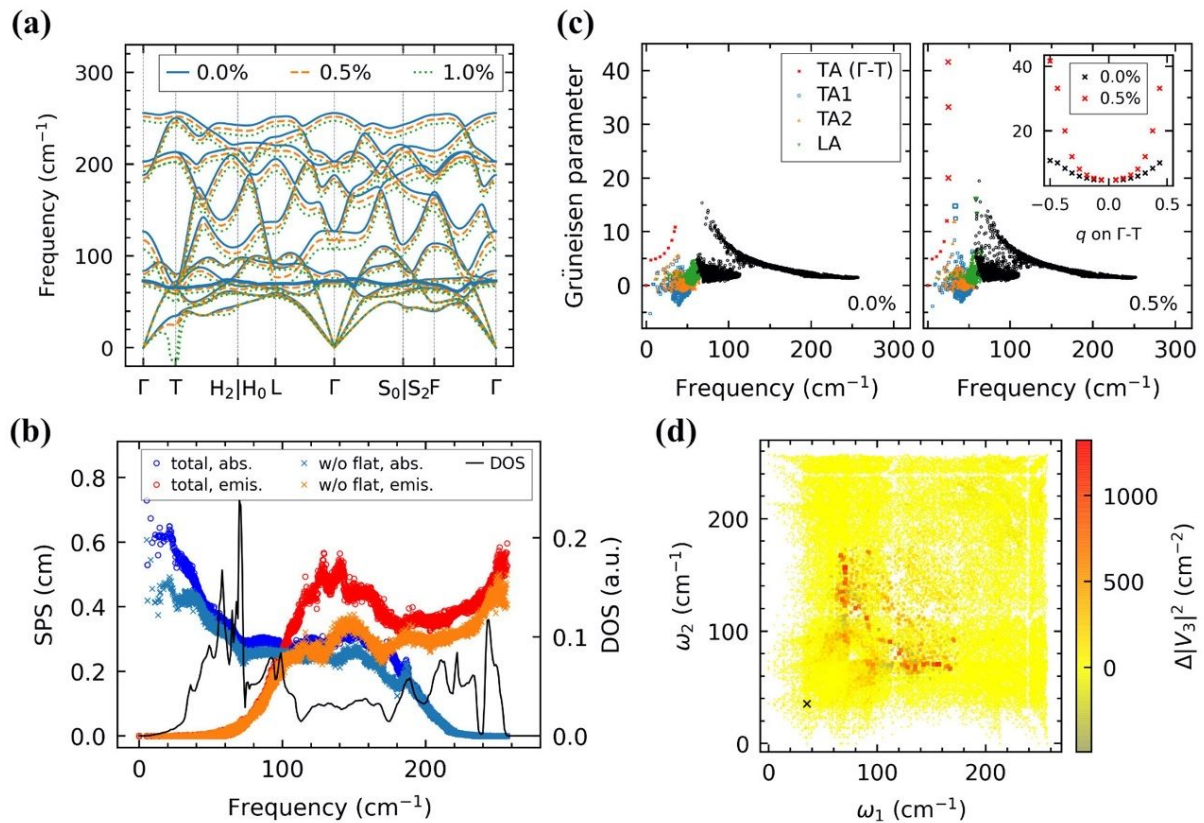
Figure 5. Phonon instability of AgBiS$_2$. (a) Phonon dispersions under hydrostatic strains (0.0, 0.5, and 1.0%). The transverse acoustic (TA) mode at T point ($q = (0.5, 0.5, 0.5)$) becomes unstable under the applied strain. The bold line around 60-80 cm^{-1} shows the lowest optical mode that significantly enhances phonon scattering. (b) Contribution of the flat band to scattering phase space (SPS). Blue and red markers show data for absorption and emission processes while circles and crosses show, respectively, the total value and the value excluding the effect of the lowest optical mode. Black line shows phonon density of states (DOS). (c) Grüneisen parameters of the pristine structure (left) and the structure under 0.5% strain (right). Red crosses show data for the TA modes along $q = (q, q, q)$, where q is an arbitrary number, corresponding to the Γ-T line and their maximum value corresponds to the T point. Inset shows data for the TA mode on Γ-T line with respect to q. (d) Change in the $|V_3|^2$ term with the 0.5% strain for the TA mode at T point, which is marked with a cross (x) in the bottom panel.

Conclusions

Two novel transport descriptors for the rapid screening of potential thermoelectric materials with high mobility and powerfactor have been introduced. Pre-existing information in Materials Project

373   database was used to filter out 12 potential candidates, and their charge transport properties have been

374   calculated and used to derive the descriptors. Inspection of the charge carrier scattering rates for this

375   family of compounds reveals that in heavily doped regime, while ionised impurities have a dominant

376   scattering contribution, polar optical phonon scattering is also important and non-negligible, and must

377   be considered for screening of new thermoelectric materials. Transport descriptors for carrier mobility

378   and powerfactor are proposed by including this new insight and validated with the literature. In

379   addition to effective mass, we proposed that dielectric constant plays an important role in determining

380   the carrier mobility and the maximum power factor. Excellent agreement with theoretical and

381   experimental data is observed, hence validating its use as first-level screening parameter in the search

382   of novel materials. In addition, the anharmonic scattering terms have been explicitly considered to

383   study the phononic thermal conductivity and the ABX_2 class of compounds are observed to be

384   promising candidates for intermediate temperature thermoelectrics.

385

Methods

386

387   The *ab initio* charge transport calculations were carried out using an Energy-dependent Phonon- and

388   Impurity-limited Carrier Scattering Time AppRoximation (EPIC STAR), a fast and reliable first

389   principles method based on density functional perturbation theory (DFPT) phonon calculation.[23]

390   QUANTUM ESPRESSO was used for DFPT calculation and the electron density of states and group

391   velocities were computed using BoltzTraP.[94] The charge transport properties were simulated by

392   considering the following effects in carrier scattering: the electron-phonon scattering from both

393   acoustic and optical, polar and nonpolar phonons, the electron-impurity scattering by ionized

394   impurities, and Thomas Fermi screening by free carriers.[23] Generalized gradient approximation with

395   exchange-correlation functional introduced by Perdew, Burke and Ernzerhof (PBE)[95] was used.

396   Pseudopotentials provided by Standard solid-state pseudopotentials (SSSP)[96] with their recommended

397   cut-off energies. 6×6×6 **k**- and **q**-point samplings are used for all compounds in their primitive cell

398   calculations.

399   For lattice thermal conductivities, contributions of diagonal and off-diagonal terms of group velocity

400   operator[97] were computed by Peierls BTE and the so-called unified theory[98] implemented in

401   ALAMODE[64], where three-phonon scattering mechanisms were included in the phonon relaxation

402   time calculation.

403   Considering the second-order perturbation within the single-mode relaxation approximation, the

404   linewidth due to the three-phonon scattering for phonon mode q, where $q = (\boldsymbol{q}, s)$ with $\boldsymbol{q}$ being the

405   wavevector and ω being the branch index is derived as:

406    $$\Gamma(\omega) = \frac{\pi}{16}\sum_{q_1,q_2}|V_3(-q, q_1, q_2)|^2 \times [(n_1 + n_2 + 1)\delta(\omega - \omega_1 - \omega_2) - 2(n_1 - n_2)\delta(\omega - \omega_1 + \omega_2)] \qquad (4)$$

407   where the subscripts ($i = 1, 2$) denote phonon modes contributing to the scattering of the target mode

408   q, ω is the phonon frequency, $n_i = 1/\{\exp(\beta\hbar\omega_i) - 1\}$ is the Bose-Einstein distribution, $\beta = k_B T$

409   with the Boltzmann constant k_B, $\hbar$ is the reduced Planck constant, N is the number of $\boldsymbol{q}$ points, and

410    $-q = (-\boldsymbol{q}, s)$. The three-phonon matrix element V_3 is given by:

411    $$V_3(q, q_1, q_2) = \left(\frac{\hbar}{N\omega\omega_1\omega_2}\right)^{1/2} \times$$

412    $$\sum_{\boldsymbol{R}_i l_i p_i} \psi_{0l_0,\boldsymbol{R}_1 l_1,\boldsymbol{R}_2 l_2}^{p_0 p_1 p_2} \times \frac{e_{l_0}^{p_0}(q)e_{l_1}^{p_1}(q_1)e_{l_2}^{p_2}(q_2)}{\sqrt{M_{l_0}M_{l_1}M_{l_2}}} \times \exp\left[i(\boldsymbol{q}\cdot\boldsymbol{R}_0 + \boldsymbol{q_1}\cdot\boldsymbol{R}_1 + \boldsymbol{q_2}\cdot\boldsymbol{R}_2)\right] \qquad (5)$$

413   where $\boldsymbol{R}_i$ is the position of the primitive cell, l_i is the atom site, p_i is the direction of the displacement

414   of atom l_i, M is the atomic mass, Ψ is the cubic IFCs, and $e(q)$ is the eigenvector of the mode q. The

415   phonon relaxation time due to three-phonon scattering τ_{pp} is given by $\tau_{pp}(q) = 1/(2\Gamma(\omega))$. The total

416   phonon relaxation time is calculated with Matthiessen's rule: $\tau_{ph}^{-1} = \tau_{pp}^1 + \tau_{iso}^{-1} + \tau_b^{-1}$, where τ_{iso}^{-1} is

417   the scattering rate due to natural isotopes, obtained with Tamura model[99], and $\tau_b^{-1} = 2|v|/L_g$ due to

418   boundaries of grains with an effective diameter L_g. Peierls contribution is calculated as $\kappa_P^{\alpha\beta}(T) =$

419    $(NV)^{-1}\sum_q c_q(T)v_q^\alpha(T)v_q^\beta(T)\tau_q(T)$, where V is the volume of the primitive unit cell, c is the mode

420   specific heat, v is the group velocity, and α and β are the Cartesian directions. In this study, the

421   averaged value of $\kappa_P^{\alpha\alpha}(T)(\alpha = x,y,z)$ was used as the Peierls contribution. Note that ABX_2 compounds

422   have slightly anisotropic lattice thermal conductivity. For example, κ_p^{zz} was 17% smaller than $\kappa_p^{xx/yy}$

423   for AgBiS$_2$ at 300 K.

424   The contribution of the wavelike coherent transport, which isassociated with the off-diagonal term of

425   the group velocity operator,was calculated with the unified theory[97,98]as:

426    $$\kappa_c^{\alpha\beta} = \frac{\hbar}{k_B^2 TVN}\sum_{\boldsymbol{q}}\sum_{s_1 \neq s_2}\frac{\omega_1 + \omega_2}{4}V_{12}^{\alpha}(\boldsymbol{q})V_{21}^{\beta}(\boldsymbol{q})\frac{\omega_1 n_1(n_1 + 1) + \omega_2 n_2(n_2 + 1)}{(\omega_1 - \omega_2)^2 + (\Gamma_1 + \Gamma_2)^2}(\Gamma_1 + \Gamma_2)$$ (6)

427   where V_{ij} is the generalized group velocity operator between eigenvector e_i and e_j. The detailed

428   documentation can be found also in elsewhere.[100]

429   The structural optimization and computation of interatomic force constants (IFCs) were conducted

430   with first-principles calculations using Vienna Ab initio Simulation Package (VASP).[101] PBEsol

431   exchange-correlation functional[102], which reproduced the lattice constant well, was employed for the

432   phonon transport analysis. Because of strong structural instability of materials[103], the structural

433   optimization of the primitive cell needed to be carefully performed with $40 \times 40 \times 40\boldsymbol{k}$-points

434   including Γ point; (a) the structural optimization was performed for structures with slightly different

435   volumes, (b) the crystal volume was determined by a parabolic fitting with respect to the volume and

436   minimized energy, and (c) the structural optimization was again performed for the structure with the

437   optimal volume. The error of the finally-obtained minimum energy and the maximum force on the

438   atoms were confirmed to be less than 0.01 meV and 0.01 meV/Å, respectively. IFCs were computed

439   with a $4 \times 4 \times 1$ supercell of rectangular conventional cell which contains 192 atoms with a finite-

440   displacement method. We have confirmed that the phonon frequency took a positive value in the

441   whole reciprocal space. Using the obtained IFCs, we have calculated phonon properties such as

442   scattering phase space (SPS), relaxation time, and lattice thermal conductivities (κ_{lat}). Thermal

443   conductivity was calculated with $16 \times 16 \times 16\boldsymbol{q}$-points.

444

445

446

Author Contributions

K. H. and S.-W.Y conceived the idea. T.D. performed the charge transport calculations. J.R.-G. performed data mining. T.D. and J.R.-G. drafted the manuscript. M.O. and J.S. computed the lattice thermal conductivities. D.V.M.R. conducted the data analysis. T.D., J.R.-G., D.V.M.R., P.K. and A.S. derived the transport descriptors. All authors contributed to the discussions and manuscript revisions.

* Denotes equal contribution

\# Authors to whom correspondence should be addressed

Conflict of Interest

The authors declare no competing interests.

Acknowledgements

References

1   J.-P. Correa-Baena, K. Hippalgaonkar, J. van Duren, S. Jaffer, V. R. Chandrasekhar, V. Stevanovic, C. Wadia, S. Guha and T. Buonassisi, *Joule*, 2018, **2**, 1410–1420.

2   B. Sanchez-Lengeling and A. Aspuru-Guzik, *Science (80-.).*, 2018, **361**, 360–365.

3   K. T. Butler, D. W. Davies, H. Cartwright, O. Isayev and A. Walsh, *Nature*, 2018, **559**, 547–555.

4   J. Zhou, H. Zhu, T.-H. Liu, Q. Song, R. He, J. Mao, Z. Liu, W. Ren, B. Liao, D. J. Singh, Z. Ren and G. Chen, *Nat. Commun.*, 2018, **9**, 1721.

5   M. W. Gaultois, A. O. Oliynyk, A. Mar, T. D. Sparks, G. J. Mulholland and B. Meredig, *APL Mater.*, 2016, **4**, 053213.

6   F. Oviedo, Z. Ren, S. Sun, C. Settens, Z. Liu, N. T. P. Hartono, S. Ramasamy, B. L. DeCost, S. I. P. Tian, G. Romano, A. Gilad Kusne and T. Buonassisi, *npj Comput. Mater.*, 2019, **5**, 60.

7   P. Gorai, V. Stevanović and E. S. Toberer, *Nat. Rev. Mater.*, 2017, **2**, 17053.

485　8　J. Yan, P. Gorai, B. Ortiz, S. Miller, S. A. Barnett, T. Mason, V. Stevanović and E. S. Toberer,
486　　　*Energy Environ. Sci.*, 2015, **8**, 983–994.

487　9　Z. M. Gibbs, F. Ricci, G. Li, H. Zhu, K. Persson, G. Ceder, G. Hautier, A. Jain and G. J.
488　　　Snyder, *npj Comput. Mater.*, 2017, **3**, 1–6.

489　10　A. Suwardi, D. Bash, H. K. Ng, J. R. Gomez, D. V. M. Repaka, P. Kumar and K.
490　　　Hippalgaonkar, *J. Mater. Chem. A*, 2019, **7**, 23762–23769.

491　11　J. J. Urban, A. K. Menon, Z. Tian, A. Jain and K. Hippalgaonkar, *J. Appl. Phys.*, ,
492　　　DOI:10.1063/1.5092525.

493　12　J. M. Ziman, *Electrons and Phonons: The Theory of Transport Phenomena in Solids*, Oxford
494　　　University Press, Oxford, 1960.

495　13　J. Yang, H. Li, T. Wu, W. Zhang, L. Chen and J. Yang, *Adv. Funct. Mater.*, 2008, **18**, 2880–
496　　　2888.

497　14　G. Samsonidze and B. Kozinsky, *Adv. Energy Mater.*, 2018, **8**, 1800246.

498　15　L. Xi, S. Pan, X. Li, Y. Xu, J. Ni, X. Sun, J. Yang, J. Luo, J. Xi, W. Zhu, X. Li, D. Jiang, R.
499　　　Dronskowski, X. Shi, G. J. Snyder and W. Zhang, *J. Am. Chem. Soc.*, 2018, **140**, 10785–
500　　　10793.

501　16　J. Bardeen and W. Shockley, *Phys. Rev.*, 1950, **80**, 72–80.

502　17　S. Li, T.-Y. Lü, J.-C. Zheng, S.-W. Yang, J.-S. Wang and G. Wu, *2D Mater.*, 2018, **5**, 035027.

503　18　X. Yong, W. Shi, G. Wu, S. S. Goh, S. Bai, J.-W. Xu, J.-S. Wang and S.-W. Yang, *J. Mater.
504　　　Chem. A*, 2018, **6**, 19757–19766.

505　19　W. Shi, G. Wu, K. Hippalgaonkar, J.-S. Wang, J. Xu and S.-W. Yang, *J. Am. Chem. Soc.*,
506　　　2018, **140**, 13200–13204.

507　20　C. Verdi and F. Giustino, *Phys. Rev. Lett.*, 2015, **115**, 176401.

508　21　P. Graziosi, C. Kumarasinghe and N. Neophytou, *ACS Appl. Energy Mater.*, 2020, **3**, 5913–
509　　　5926.

510　22　P. Graziosi, C. Kumarasinghe and N. Neophytou, *J. Appl. Phys.*, 2019, **126**, 155701.

511　23　T. Deng, G. Wu, M. B. Sullivan, Z. M. Wong, K. Hippalgaonkar, J.-S. Wang and S.-W. Yang,
512　　　*npj Comput. Mater.*, 2020, **6**, 46.

513　24　F. Giustino, M. L. Cohen and S. G. Louie, *Phys. Rev. B - Condens. Matter Mater. Phys.*, 2007,
514　　　**76**, 1–19.

515　25　S. Poncé, E. R. Margine, C. Verdi and F. Giustino, *Comput. Phys. Commun.*, 2016, **209**, 116–
516　　　133.

517　26　J. Ma, A. S. Nissimagoudar and W. Li, *Phys. Rev. B*, 2018, **97**, 045201.

518　27　S. Poncé, E. R. Margine and F. Giustino, *Phys. Rev. B*, 2018, **97**, 121201.

519　28　T. Deng, X. Yong, W. Shi, C. K. Gan, W. Li, K. Hippalgaonkar, J. Zheng, X. Wang, S. Yang,
520　　　J. Wang and G. Wu, *Adv. Electron. Mater.*, 2019, **5**, 1800892.

521　29　W. Shi, T. Deng, G. Wu, K. Hippalgaonkar, J. Wang and S. Yang, *Adv. Mater.*, 2019, **31**,
522　　　1901956.

523　30　J.-J. Zhou and M. Bernardi, *Phys. Rev. B*, 2016, **94**, 201201.

524　31　T.-H. Liu, J. Zhou, B. Liao, D. J. Singh and G. Chen, *Phys. Rev. B*, 2017, **95**, 075206.

525   32   G. Brunin, H. P. C. Miranda, M. Giantomassi, M. Royo, M. Stengel, M. J. Verstraete, X.
526   Gonze, G.-M. Rignanese and G. Hautier, .

527   33   P. R. Raghuvanshi, S. Mondal and A. Bhattacharya, *J. Mater. Chem. A*, 2020, **8**, 25187–
528   25197.

529   34   R. Gautier, X. Zhang, L. Hu, L. Yu, Y. Lin, T. O. L. Sunde, D. Chon, K. R. Poeppelmeier and
530   A. Zunger, *Nat. Chem.*, 2015, **7**, 308–316.

531   35   H. Zhu, J. Mao, Y. Li, J. Sun, Y. Wang, Q. Zhu, G. Li, Q. Song, J. Zhou, Y. Fu, R. He, T.
532   Tong, Z. Liu, W. Ren, L. You, Z. Wang, J. Luo, A. Sotnikov, J. Bao, K. Nielsch, G. Chen, D.
533   J. Singh and Z. Ren, *Nat. Commun.*, 2019, **10**, 270.

534   36   F. Ricci, A. Dunn, A. Jain, G.-M. Rignanese and G. Hautier, *J. Mater. Chem. A*, 2020, **8**,
535   17579–17594.

536   37   T. Jia, Z. Feng, S. Guo, X. Zhang and Y. Zhang, *ACS Appl. Mater. Interfaces*, 2020, **12**,
537   11852–11864.

538   38   S. Sarikurt, T. Kocabaş and C. Sevik, *J. Mater. Chem. A*, 2020, **8**, 19674–19683.

539   39   R. Li, X. Li, L. Xi, J. Yang, D. J. Singh and W. Zhang, *ACS Appl. Mater. Interfaces*, 2019, **11**,
540   24859–24866.

541   40   A. Jain, S. P. Ong, G. Hautier, W. Chen, W. D. Richards, S. Dacek, S. Cholia, D. Gunter, D.
542   Skinner, G. Ceder and K. A. Persson, *APL Mater.*, 2013, **1**, 011002.

543   41   Z. M. Gibbs, H.-S. Kim, H. Wang and G. J. Snyder, *Appl. Phys. Lett.*, 2015, **106**, 022112.

544   42   M. D. Nielsen, V. Ozolins and J. P. Heremans, *Energy Environ. Sci.*, 2013, **6**, 570–578.

545   43   J. Recatala-Gomez, A. Suwardi, I. Nandhakumar, A. Abutaha and K. Hippalgaonkar, *ACS*
546   *Appl. Energy Mater.*, 2020, **3**, 2240–2257.

547   44   H. J. Goldsmid and J. W. Sharp, 1999, **28**, 1–4.

548   45   H. Xiao, Y. Dan, B. Suo and X. Chen, *J. Phys. Chem. C*, 2020, **124**, 2247–2249.

549   46   S. Kim, J. Noh, G. H. Gu, A. Aspuru-Guzik and Y. Jung, *ACS Cent. Sci.*, 2020, **6**, 1412–1420.

550   47   E. Rathore, R. Juneja, S. P. Culver, N. Minafra, A. K. Singh, W. G. Zeier and K. Biswas,
551   *Chem. Mater.*, 2019, **31**, 2106–2113.

552   48   Y. Pei, X. Shi, A. LaLonde, H. Wang, L. Chen and G. J. Snyder, *Nature*, 2011, **473**, 66–69.

553   49   S. I. Kim, K. H. Lee, H. A. Mun, H. S. Kim, S. W. Hwang, J. W. Roh, D. J. Yang, W. H. Shin,
554   X. S. Li, Y. H. Lee, G. J. Snyder and S. W. Kim, *Science (80-.).*, 2015, **348**, 109–114.

555   50   J. P. Heremans, V. Jovovic, E. S. Toberer, A. Saramat, K. Kurosaki, A. Charoenphakdee, S.
556   Yamanaka and G. J. Snyder, *Science (80-.).*, 2008, **321**, 554–557.

557   51   J. Mao, H. Zhu, Z. Ding, Z. Liu, G. A. Gamage, G. Chen and Z. Ren, *Science (80-.).*, 2019,
558   **365**, 495–498.

559   52   C. Chang, M. Wu, D. He, Y. Pei, C.-F. Wu, X. Wu, H. Yu, F. Zhu, K. Wang, Y. Chen, L.
560   Huang, J.-F. Li, J. He and L.-D. Zhao, *Science (80-.).*, 2018, **360**, 778–783.

561   53   W. He, D. Wang, H. Wu, Y. Xiao, Y. Zhang, D. He, Y. Feng, Y.-J. Hao, J.-F. Dong, R.
562   Chetty, L. Hao, D. Chen, J. Qin, Q. Yang, X. Li, J.-M. Song, Y. Zhu, W. Xu, C. Niu, X. Li, G.
563   Wang, C. Liu, M. Ohta, S. J. Pennycook, J. He, J.-F. Li and L.-D. Zhao, *Science (80-.).*, 2019,
564   **365**, 1418–1424.

565   54   S. R. Shinde, S. B. Ogale, J. S. Higgins, H. Zheng, A. J. Millis, V. N. Kulkarni, R. Ramesh, R.

566   L. Greene and T. Venkatesan, *Phys. Rev. Lett.*, 2004, **92**, 166601.

567   55   J. Li, X. Zhang, Z. Chen, S. Lin, W. Li, J. Shen, I. T. Witting, A. Faghaninia, Y. Chen, A. Jain,
568   L. Chen, G. J. Snyder and Y. Pei, *Joule*, 2018, 1–12.

569   56   F. Ricci, W. Chen, U. Aydemir, J. Snyder, G. Rignanese, A. Jain and G. Hautier, *Sci. Data*,
570   2017, **4**, 170085.

571   57   K. Kurosaki, A. Kosuga and S. Yamanaka, *J. Alloys Compd.*, 2003, **351**, 279–282.

572   58   J. D. Jensen, J. R. Burke, D. W. Ernst and R. S. Allgaier, *Phys. Rev. B*, 1972, **6**, 319–327.

573   59   T. Sato, K. Segawa, H. Guo, K. Sugawara, S. Souma, T. Takahashi and Y. Ando, *Phys. Rev.*
574   *Lett.*, 2010, **105**, 1–4.

575   60   N. S. Popovich, *Mold. J. Phys. Sci.*, 2003, **2**, N2.

576   61   Y. Shi, Q. Guo, X. Cheng, P. Jafarzadeh, L. R. Macario, L. Menezes and H. Kleinke, *J. Alloys*
577   *Compd.*, 2019, **795**, 1–7.

578   62   S. Geller and J. H. Wernick, *Acta Crystallogr.*, 1959, **12**, 46–54.

579   63   C. Manolikas and J. Spyridelis, *Mater. Res. Bull.*, 1977, **12**, 907–913.

580   64   T. Tadano, Y. Gohda and S. Tsuneyuki, *J. Phys. Condens. Matter*, 2014, **26**, 225402.

581   65   P. Norouzzadeh, C. W. Myles and D. Vashaee, *Phys. Rev. B*, 2017, **95**, 1–9.

582   66   K. Pal, Y. Xia, J. He and C. Wolverton, *Chem. Mater.*, 2019, **31**, 8734–8741.

583   67   A. Walsh, D. J. Payne, R. G. Egdell and G. W. Watson, *Chem. Soc. Rev.*, 2011, **40**, 4455–
584   4463.

585   68   M. Hong, Z.-G. Chen, L. Yang, Z.-M. Liao, Y.-C. Zou, Y.-H. Chen, S. Matsumura and J. Zou,
586   *Adv. Energy Mater.*, 2018, **8**, 1702333.

587   69   S. Roychowdhury, T. Ghosh, R. Arora, M. Samanta, L. Xie, N. K. Singh, A. Soni, J. He, U. V
588   Waghmare and K. Biswas, *Science (80-.).*, 2021, **371**, 722–727.

589   70   Y. Pei, A. D. LaLonde, H. Wang and G. J. Snyder, *Energy Environ. Sci.*, 2012, **5**, 7963.

590   71   L.-D. Zhao, S.-H. Lo, J. He, H. Li, K. Biswas, J. Androulakis, C.-I. Wu, T. P. Hogan, D.-Y.
591   Chung, V. P. Dravid and M. G. Kanatzidis, *J. Am. Chem. Soc.*, 2011, **133**, 20476–20487.

592   72   J. S. G. Wang H., Pei Y., LaLonde A.D., *Material Design Considerations Based on*
593   *Thermoelectric Quality Factor*, Springer Berlin Heidelberg, Berlin, Heidelberg, 2013, vol.
594   182.

595   73   J. Sjakste, N. Vast, M. Calandra and F. Mauri, *Phys. Rev. B*, 2015, **92**, 054307.

596   74   M. Lundstrom, *Fundamentals of Carrier Transport*, Cambridge University Press, Cambridge,
597   2000.

598   75   S. Perumal, M. Samanta, T. Ghosh, U. S. Shenoy, A. K. Bohra, S. Bhattacharya, A. Singh, U.
599   V. Waghmare and K. Biswas, *Joule*, 2019, **3**, 2565–2580.

600   76   In *Non-Tetrahedrally Bonded Elements and Binary Compounds I*, Springer-Verlag,
601   Berlin/Heidelberg, vol. 0, pp. 1–3.

602   77   H. A. Lyden, *Phys. Rev.*, 1964, **135**, A514–A521.

603   78   T. Zhu, Y. Liu, C. Fu, J. P. Heremans, J. G. Snyder and X. Zhao, *Adv. Mater.*, ,
604   DOI:10.1002/adma.201605884.

605 79   A. Ioffe, *Semiconductor Thermoelements and Thermoelectric Cooling*, Infosearch, Lodon,
606   1957.

607 80   M. Hong, W. Lyu, Y. Wang, J. Zou and Z. G. Chen, *J. Am. Chem. Soc.*, 2020, **142**, 2672–
608   2681.

609 81   S. Lin, W. Li, Z. Chen, J. Shen, B. Ge and Y. Pei, *Nat. Commun.*, 2016, **7**, 1–6.

610 82   C. B. Vining, *J. Appl. Phys.*, 1991, **69**, 331–341.

611 83   O. Yamashita and N. Sadatomi, *Japanese J. Appl. Physics, Part 1 Regul. Pap. Short Notes*
612   *Rev. Pap.*, 1999, **38**, 6394–6400.

613 84   Y. Cao, X. Su, F. Meng, T. P. Bailey, J. Zhao, H. Xie, J. He, C. Uher and X. Tang, *Adv. Funct.*
614   *Mater.*, 2020, 2005861.

615 85   T. Plirdpring, K. Kurosaki, A. Kosuga, T. Day, S. Firdosy, V. Ravi, G. J. Snyder, A.
616   Harnwunggmoung, T. Sugahara, Y. Ohishi, H. Muta and S. Yamanaka, *Adv. Mater.*, 2012, **24**,
617   3622–3626.

618 86   S. K. Bux, R. G. Blair, P. K. Gogna, H. Lee, G. Chen, M. S. Dresselhaus, R. B. Kaner and J. P.
619   Fleurial, *Adv. Funct. Mater.*, 2009, **19**, 2445–2452.

620 87   D. S. Parker, A. F. May and D. J. Singh, *Phys. Rev. Appl.*, 2015, **3**, 064003.

621 88   P. Pichanusakorn and P. Bandaru, *Mater. Sci. Eng. R Reports*, 2010, **67**, 19–63.

622 89   P. Pichanusakorn and P. R. Bandaru, *Appl. Phys. Lett.*, 2009, **94**, 223108.

623 90   X. Zhang, Z. Bu, X. Shi, Z. Chen, S. Lin, B. Shan, M. Wood, A. H. Snyder, L. Chen, G. J.
624   Snyder and Y. Pei, 2020, 6–11.

625 91   W. Li and N. Mingo, *Phys. Rev. B*, 2014, **89**, 184304.

626 92   W. Li and N. Mingo, *Phys. Rev. B*, 2015, **91**, 144304.

627 93   T. Tadano, Y. Gohda and S. Tsuneyuki, *Phys. Rev. Lett.*, 2015, **114**, 095501.

628 94   G. K. H. Madsen and D. J. Singh, *Comput. Phys. Commun.*, 2006, **175**, 67–71.

629 95   J. P. Perdew, K. Burke and M. Ernzerhof, *Phys. Rev. Lett.*, 1996, **77**, 3865–3868.

630 96   G. Prandini, A. Marrazzo, I. E. Castelli, N. Mounet and N. Marzari, *npj Comput. Mater.*, 2018,
631   **4**, 72.

632 97   R. J. Hardy, *Phys. Rev.*, 1963, **132**, 168–177.

633 98   M. Simoncelli, N. Marzari and F. Mauri, *Nat. Phys.*, 2019, **15**, 809–813.

634 99   S. Tamura, *Phys. Rev. B*, 1983, **27**, 858–866.

635 100 M. Ohnishi, T. Tadano, S. Tsuneyuki and J. Shiomi, 2021, 15–17.

636 101 G. Kresse and J. Hafner, *Phys. Rev. B*, 1993, **47**, 558–561.

637 102 G. I. Csonka, J. P. Perdew, A. Ruzsinszky, P. H. T. Philipsen, S. Lebègue, J. Paier, O. A.
638   Vydrov and J. G. Ángyán, *Phys. Rev. B*, 2009, **79**, 155107.

639 103 A.   Togo,   Phonon   database   at   2018-04-17,   http://phonondb.mtl.kyoto-
640   u.ac.jp/ph20180417/index.html, (accessed 19 November 2020).

641